SDU
University of Southern Denmark

Polarization wake of penetrating ions: Oscillator model

Sigmund, Peter; Schinner, Andreas

Published in:
The European Physical Journal D

DOI:
10.1140/epjd/e2012-20761-9

Publication date:
2012

Citation for pulished version (APA):
Sigmund, P., & Schinner, A. (2012). Polarization wake of penetrating ions: Oscillator model. *The European Physical Journal D*, *66*(56), 1-11. https://doi.org/10.1140/epjd/e2012-20761-9

Go to publication entry in University of Southern Denmark's Research Portal

Terms of use
This work is brought to you by the University of Southern Denmark.
Unless otherwise specified it has been shared according to the terms for self-archiving.
If no other license is stated, these terms apply:

- You may download this work for personal use only.
- You may not further distribute the material or use it for any profit-making activity or commercial gain
- You may freely distribute the URL identifying this open access version

If you believe that this document breaches copyright please contact us providing details and we will investigate your claim.
Please direct all enquiries to puresupport@bib.sdu.dk

Download date: 11. Jan. 2025

EPJ manuscript No.
(will be inserted by the editor)

Polarization Wake of Penetrating Ions: Oscillator model

Andreas Schinner[1] and Peter Sigmund[2]

[1] Institut für Experimentalphysik, Johannes Kepler Universität, A-4040 Linz-Auhof, Austria
[2] Department of Physics, Chemistry and Pharmacy, University of Southern Denmark, DK-5230 Odense M, Denmark

Received:

Abstract. The wake potential induced by a swift nonrelativistic ion has been studied theoretically for a random stopping medium consisting of quantal-harmonic-oscillator atoms. The primary purpose has been to study the influence of atomic binding on the frequently-studied wake potential in a Fermi gas. Quantitative comparisons at constant plasma frequency and increasing oscillator frequency show a gradual decrease in wavelength and a slight decrease in amplitude of the oscillatory part of the wake potential, as well as a systematic decrease in screening of the near-field next to the projectile. These findings can be expected on the basis of the Drude-Lorentz formula for the effective resonance frequency. We find a distinct dependence of the induced potential on the ion charge as long as the plasma frequency exceeds the oscillator frequency. In the opposite case of a dominating oscillator frequency we find little difference between the field induced by a point charge and that by a neutral atom. As an application area we briefly discuss the proximity effect in the energy loss of molecular ions. We find that the polarization wake *modifies* the proximity effect, in contrast to the frequently-expressed view that it *causes* the proximity effect.

PACS. 34.50.Bw; and 71.45.Gm;

1 Introduction

In 1940 Fermi [1] pointed out that a swift charged particle traversing condensed matter carries with it an induced electromagnetic field which gives rise to a significant reduction in the energy loss (Fermi density effect). Early studies of this 'wake' [2] field focused on particles moving at relativistic velocities [1, 3, 4]. Neufeld and Ritchie [5] demonstrated that significant polarization of the stopping medium also may be expected at nonrelativistic projectile speeds, and they derived an explicit expression for the wake potential on the basis of the Drude-Lorentz model of a conducting medium.

The wake phenomenon received considerable interest in connection with experimental observations on the penetration of swift molecules and clusters [6–9]. Theoretical estimates were based on the Lindhard scheme [10], and the stopping medium was modeled mostly as a Fermi gas, either by the Lindhard dielectric function or modifications thereof [6, 11–14]. Extensions beyond these schemes include a first-order theory involving bound electrons in a lattice [15] and a second-order correction to the wake potential of a Fermi gas [16].

While the Fermi gas is an illuminating model system to study stopping phenomena in general, we find its dominance in the description of the polarization wake somewhat surprising. After all, the polarization vector in *electrostatics* conventionally characteristizes the state of an insulating material. In the study of time-dependent fields the difference between the response of free and bound electrons may be less pronounced than in equilibrium, but to the best of our knowledge, significance and magnitude of the difference and its dependence on beam and target parameters are largely unknown.

The present study is based upon a quantal extension of the classical Drude-Lorentz insulator. Unlike the Fermi gas, which is uniquely defined by the density of free electrons, the Drude-Lorentz model operates with at least two independent parameters, one or more binding frequencies ω_j and a plasma frequency ω_p, the latter characterizing the electron density. It is the interplay between these parameters that may give insight into the above problematics, and studying a system with just one binding frequency ought to produce a transparent picture.

The Drude-Lorentz theory describes long-wavelength polarization phenomena and, therefore, breaks down near the trajectory, where the induced field is most pronounced. It is necessary, therefore, to utilize a description that describes variations over short wavelengths in a consistent manner. An appropriate tool here is the dielectric function $\epsilon(k, \omega)$ based on the linear response of a 3D quantum oscillator, as derived in ref. [17] on the basis of refs. [10] and [18].

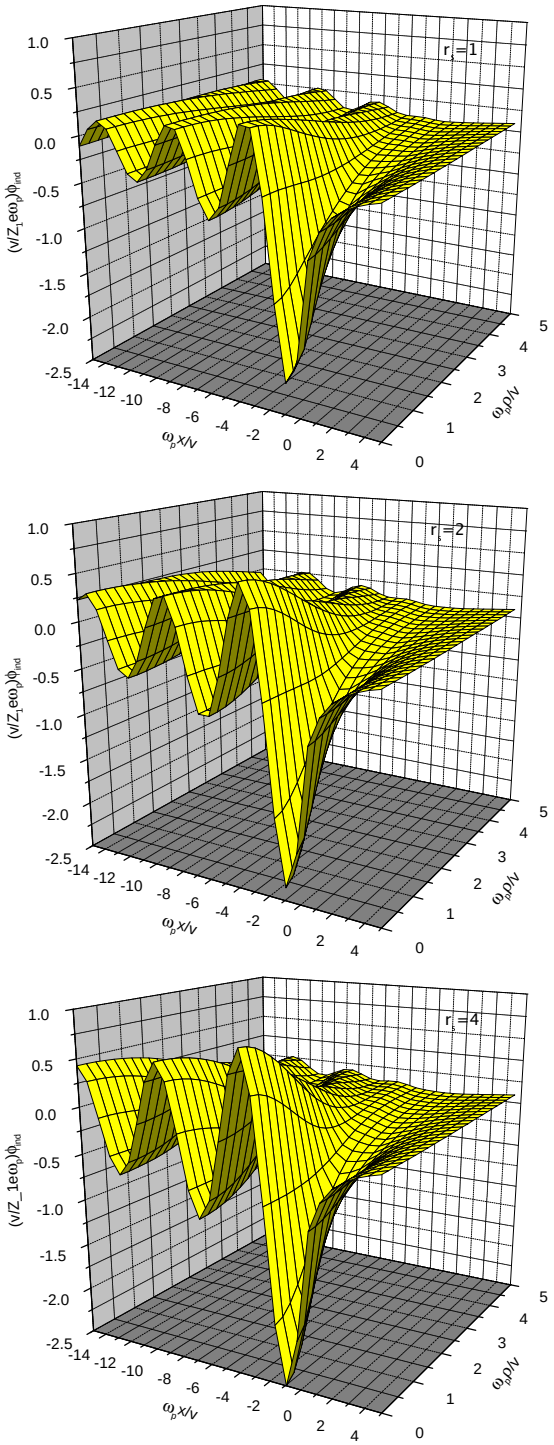

Fig. 1. Induced potential for Fermi gas at $2mv^2/\hbar\omega_p = 10$ and $r_s = 1, 2, 4$ (top to bottom).

2 Recapitulation

2.1 Induced Potential

According to Lindhard [10] the longitudinal field induced by a point charge $Z_1 e$ moving with a speed $v \ll c$ in a medium characterized by a dielectric function $\epsilon(k,\omega)$ may be expressed by a potential

$$\Phi_{\rm ind}(\boldsymbol{r},t) = \frac{Z_1 e}{2\pi^2}\int \frac{d^3\boldsymbol{k}}{k^2} e^{i\boldsymbol{k}\cdot(\boldsymbol{r}-\boldsymbol{v}t)}\left(\frac{1}{\epsilon(k,\omega)}-1\right). \quad (1)$$

In a reference frame moving with the projectile this may be written in the form [5]

$$\Phi_{\rm ind}(x,\rho) = \frac{Z_1 e}{\pi}\int_0^\infty k\,dk\,J_0(k\rho)\int_{-\infty}^{\infty}\frac{e^{i\kappa x}\,d\kappa}{k^2+\kappa^2} \times\left(\frac{1}{\epsilon\left(\sqrt{k^2+\kappa^2},\kappa v\right)}-1\right) \quad (2)$$

in terms of cylindric cordinates $(x,\boldsymbol{\rho})$, where J_0 indicates a Bessel function in standard notation [19].

2.2 Fermi Gas

Numerous graphs from the literature show wake potentials calculated from this or related models [12]. Figure 1 shows induced potentials evaluated numerically from eq. (2) by inserting the standard Lindhard function [10], which is charaterized by an electron density n, expressed here by the Wigner-Seitz radius r_s. Even though the electron density varies strongly, decreasing as 64:8:1 from top to bottom, the three plots look rather similar, indicating that the main effect of the density variation is taken care of by the scaling variables denoting the axes. It appears justified, therefore, in the following to ignore this difference and, for definiteness, to operate with the potential for $r_s = 2$.

2.3 Classical Oscillator

Another option is based on the Drude-Lorentz dielectric function for an ensemble of harmonic oscillators with a resonance frequency ω_0 [20],

$$\epsilon(k,\omega) \equiv \epsilon(\omega) = 1 + \frac{\omega_p^2}{\omega_0^2-\omega^2-i\gamma\omega}, \quad (3)$$

where γ is an infinitesimal positive constant. In that case, the integral in eq. (1) reduces to [5]

$$\phi_{\rm ind} = \phi_{\rm ind}^{(1)} + \phi_{\rm ind}^{(2)} \quad (4)$$

with

$$\phi_{\rm ind}^{(1)} = -\frac{Z_1 e\omega_p^2}{v^2}\int_0^\infty \frac{dk}{k^2+\omega'^2/v^2}\,J_0(k\rho)\,e^{-k|x|} \quad (5)$$

for all x, and

$$\phi_{\rm ind}^{(2)} = \frac{2Z_1 e\omega_p^2}{v\omega'}\sin\left(\frac{\omega' x}{v}\right)K_0\left(\frac{\omega'}{v}\rho\right) \quad (6)$$

for $x < 0$, where

$$\omega' = \sqrt{\omega_p^2+\omega_0^2}, \quad (7)$$

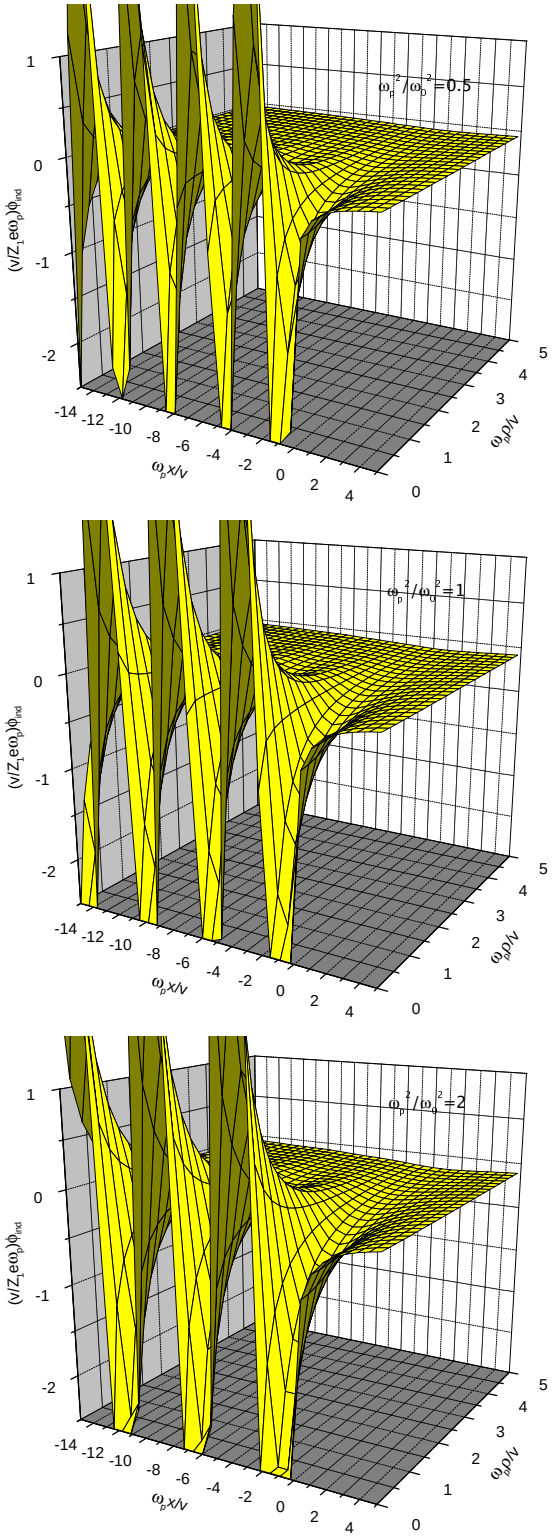

Fig. 2. Induced potential for a medium of classical oscillators at $2mv^2/\hbar\omega_p = 10$ and $\omega_p^2/\omega_0^2 = 0.5, 1, 2$ (top to bottom).

and $K_0(z)$ is a modified Bessel function in standard notation [19].

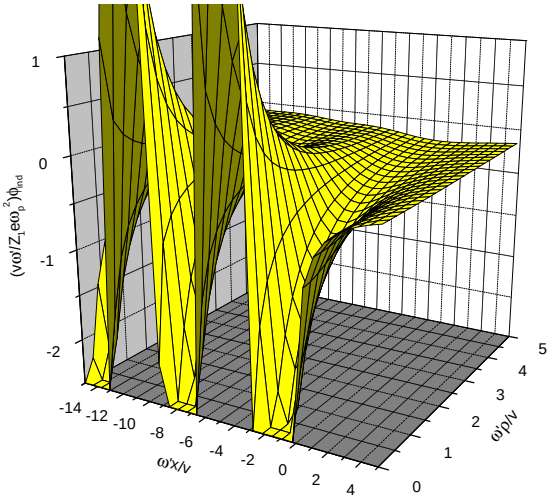

Fig. 3. Replot of figure 2 in terms of the effective resonance frequency ω' defined by eq. (7).

In figure 2 the function $\phi_{\rm ind}(x,\rho)$ has been plotted in terms of the same variables as in figure 1. It is seen that both the magnitude of the field and the oscillation period are sensitive to the oscillator frequency ω_0. However, the proper frequency unit here is ω' according to eqs. (5) and (6). Figure 3 represents all three plots from figure 2 in appropriate scaled variables.

Equations (4) - (6) are based on a long-wavelength description of the induced field. Therefore the range of validity is restricted to not too small distances ρ from the trajectory. This is manifested in a sharp increase seen in figure 2 and divergencies of eqs. (5) and (6) at $\rho = 0$.

3 Quantum Oscillator

According to ref. [17] the dielectric function of a random assembly of quantum oscillators is given as

$$\epsilon(k,\omega) = 1 + \frac{\omega_p^2}{2\omega_k}\, e^{-\omega_k/\omega_0} \sum_{n=1}^{\infty} \frac{1}{n!} \left(\frac{\omega_k}{\omega_0}\right)^n \times \\ \times \left(\frac{1}{n\omega_0 - \omega - i\gamma} + \frac{1}{n\omega_0 + \omega + i\gamma}\right), \quad (8)$$

where $\omega_k = \hbar k^2/2m$.

The analytic structure (an infinite number of zeroes, each located between two poles) of eq. (8) requires full numerical evaluation of the double integral eq. (2). It is not possible to simplify the inner integral along the κ-axis by applying the residue theorem, since an infinite number of additional non-trivial residues are present in the complex κ-plane.

Let $\kappa_j = \omega_j/v$ denote the j-th positive zero of $\epsilon(k,\omega)$. Then, using the Kramers-Kronig relation to express the real part (ϵ_1) of eq. (8) via its imaginary part, eq. (2) can be rewritten as

$$\Phi(x,\rho) = 2Z_1 e \sum_j \int_0^\infty \frac{dk}{k} \Lambda_j(k,x,\rho) \quad (9)$$

where

$$\Lambda_j(k,x,\rho) = \left|\frac{\partial\epsilon_1}{\partial\kappa}\right|^{-1}_{\kappa_j} \{I_j(k,x,\rho) + F_j(\kappa_j,k,\rho)\left[g_j(k,x) + \Theta(k-\kappa_j)\sin(\kappa_j x)\right]\} \quad (10)$$

and

$$I_j(k,x,\rho) = \frac{1}{\pi}\int_0^k d\kappa\ \cos(\kappa x)\frac{F_j(\kappa)-F_j(\kappa_j)}{\kappa-\kappa_j}, \quad (11)$$

$$F_j(\kappa,k,\rho) = \frac{2\kappa_j}{\kappa+\kappa_j}\,J_0\left(\sqrt{|k^2-\kappa^2|}\,\rho\right), \quad (12)$$

$$g_j(k,x) = \frac{1}{\pi}\cos(\kappa_j x)\big[\mathrm{Ci}(\kappa_j x - kx) - \mathrm{Ci}(\kappa_j x)\big] + \frac{1}{\pi}\sin(\kappa_j x)\big[\mathrm{Si}(\kappa_j x - kx) - \mathrm{Si}(\kappa_j x)\big]. \quad (13)$$

In the definition of eq. (11) the arguments k and ρ of F_j have been omitted for brevity; Si and Ci denote the integral sine and cosine, respectively. The discontinuities of the k-integrand Λ_j are contained in the step function Θ and in the logarithmic singularity for $k \to \kappa_j$ of $g_j(k,x)$. This separation is essential for numerical performance and stability.

The upper summation limit $j_{\max}$ in eq. (9) has been determined dynamically, i.e., the summation stops as soon as a term contributes less than 10^{-9} times the sum acquired so far. However, to avoid spurious convergence, $j_{\max}$ has not been allowed to fall below 10. Depending on the parameters, typical values for $j_{\max}$ lie between 20 and 100.

Equation (9) represents a decomposition of the wake potential into partial contributions from an infinite number of individual oscillator excitations. Behind the projectile ($x < 0$) each term will show a more or less regular oscillatory behavior, characterized by a wave number very roughly given by $k_j \approx j\omega_0/v$. However, interference patterns will emerge from the superposition eq. (9), in particular for high projectile speed and sufficiently large $(-x)$.

Numerical evaluation leads to potentials shown in figure 4, which can be compared directly with figure 2. Equivalent graphs show mutual agreement as far as the oscillation period and the behavior at large values of ρ are concerned, while the behavior close to the trajectory has now become regular.

Figure 5 shows the same data replotted in terms of the variables appropriate to the classical Drude-Lorentz oscillator, figure 3. It is seen that this renders the oscillation period almost independent of ω_p^2/ω_0^2. As it must be, the three potentials are in complete agreement at large values of ρ, while a minor difference remains close to the trajectory.

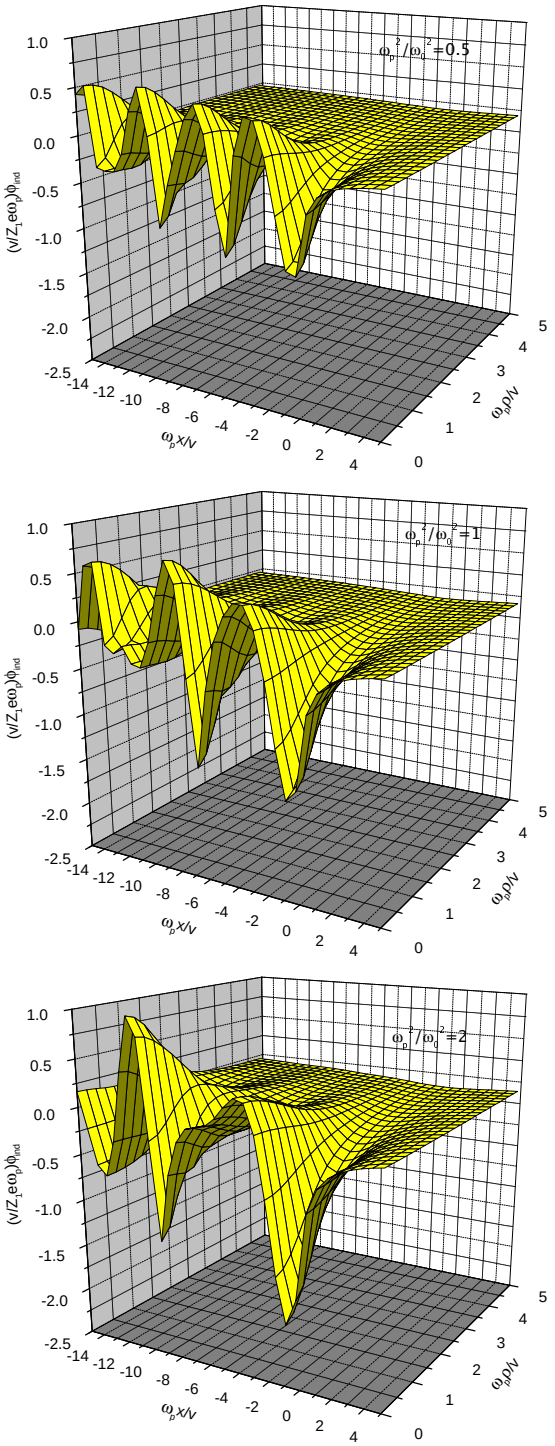

Fig. 4. Induced potential for a medium of quantum oscillators at $2mv^2/\hbar\omega_p = 10$ and $\omega_p^2/\omega_0^2 = 0.5, 1, 2$ (top to bottom). Length scale as in figures 1 and 2.

4 Preliminary Discussion

Having identified approximate scaling properties of the induced potential for an ensemble of quantum oscillators we are ready to come back to the question asked in the introduction: How does electron binding affect the wake potential of an electron gas?

This may be found by comparing figure 4 with figure 1. Note first that both graphs refer to the same ion velocity expressed by $2mv^2/\hbar\omega_p = 10$, and that the same units

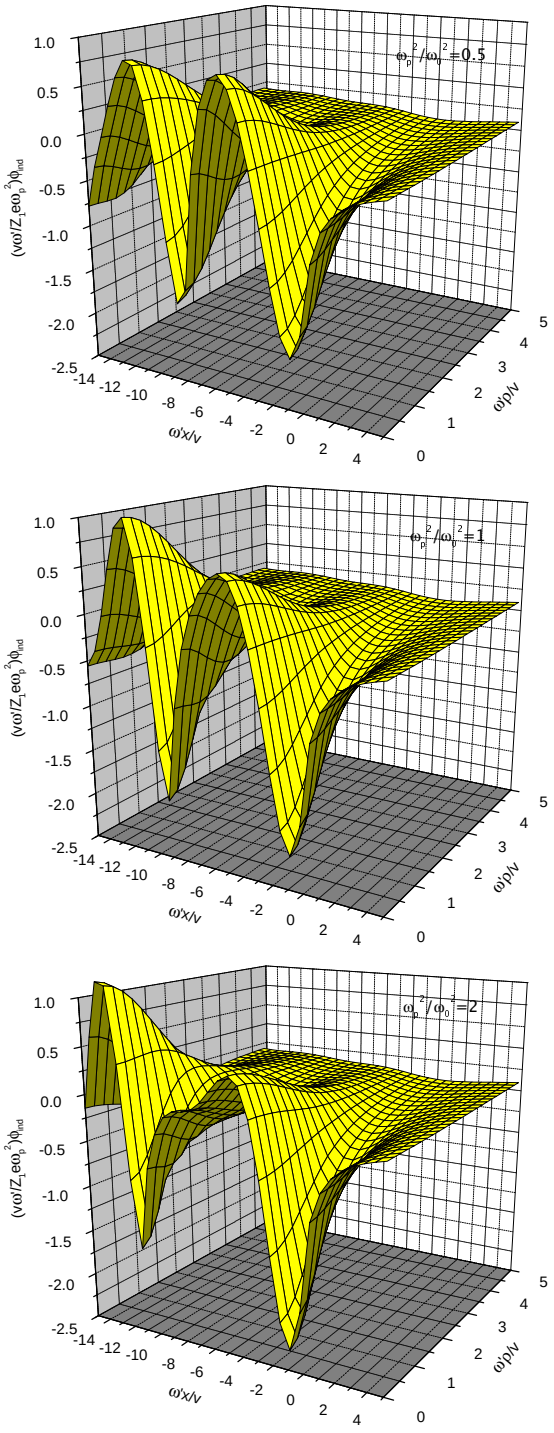

Fig. 5. Figure 4 replotted in terms of variables as in figure 3.

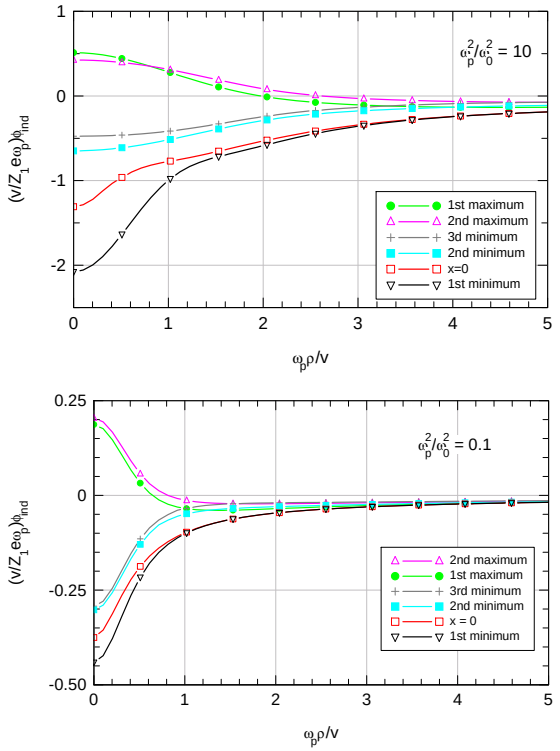

Fig. 8. Lateral variation of the induced potential for $B = 2mv^2/\hbar\omega_p = 10$ in the position of the ion $x = 0$ as well as in the longitudinal positions corresponding to maxima and minima closest to the ion.

have been applied in equivalent axes. Ignoring small differences between the three graphs in figure 1, we notice that the bottom graph in figure 4 is most similar to figure 1. In this case we have $\omega_p^2 > \omega_0^2$. In the opposite case, the top graph in figure 4, where $\omega_p^2 < \omega_0^2$, the oscillation frequency is greater and the oscillation amplitude is smaller.

5 Results

5.1 The Core Potential

While the qualitative behavior of the wake potential can be illustrated by 3D graphs, details show up more directly in two dimensions. Here we first consider the potential in the very trajectory, i.e., for $\rho = 0$. Although we have learned that ω' is the effective resonance frequency to represent the induced potential in an almost universal plot, units involving the plasma frequency ω_p are employed here in order to illustrate deviations from the Fermi-gas description of a wake.

Figure 6 shows induced potentials for the Fermi gas and ensembles of oscillators for $B = 2mv^2/\hbar\omega_p = 10$. Outstanding features are the behavior near the projectile ($x = 0$) on the one hand, and far behind the projectile (negative x) on the other.

For the Fermi gas (upper left graph) we observe pronounced asymmetric screening of the Coulomb potential near $x = 0$. A very similar screening effect is found for the oscillator for $\omega_p^2/\omega_0^2 = 10$. It decreases slowly as the ratio ω_p^2/ω_0^2 decreases down to $\simeq 1$, from where it decreases more rapidly to become insignificant at $\omega_p^2/\omega_0^2 \simeq 0.1$. A very similar behavior has been found for $B = 2mv^2/\hbar\omega_p = 20$ and 5.0 (not shown).

The oscillatory part of the induced potential shows a different behavior. Firstly, at all values of ω_p^2/ω_0^2 the in-

duced potential appears to dominate over the Coulomb potential behind the first maximum. Next, a gradual transition is seen from an oscillation governed by the plasma frequency to the opposite case of a more rapid oscillation governed primarily by the oscillator frequency for $\omega_p^2/\omega_0^2 \ll 1$. Thirdly, interferences occur which may be destructive at intermediate values of ω_p^2/ω_0^2, as seen e.g. for $\omega_p^2/\omega_0^2 = 2$. Lastly, distinct oscillations are seen also for $\omega_p^2/\omega_0^2 = 0.1$, albeit with a comparatively small amplitude and a higher frequency, compared to the Fermi gas.

In two of the graphs ($\omega_p^2/\omega_0^2 = 10$ and 0.1) we have included an additional curve indicated by crosses, which reflects the leading term $j = 1$ in eq. (9). This illustrates the fact that the convergence of the series in eq. (9) becomes increasingly slow as ω_p^2/ω_0^2 increases.

Note that restriction to $j = 1$ in eq. (9) is by no means equivalent with restriction of the sum in eq. (8) to $n = 1$. That approximation reduces the dielectric function to the Drude-Lorentz function cut off at $\omega_k \simeq \omega_0$. This approximation is equivalent with the distant part of Bethe stopping theory, i.e., it would underestimate the stopping force by about a factor of two.

5.2 Lateral Variation

Figure 7 shows the variation of the potential at $x = 0$ in the lateral direction for $2mv^2/\hbar\omega_p = 10$, which can be compared to four of the longitudinal variations shown in figure 6. As regards the behavior in the vicinity of the ion, i.e., for $\omega_p\rho/v \ll 1$, the conclusions are very similar to those drawn from figure 6. In particular, screening of the Coulomb potential appears negligible for $\omega_p^2/\omega_0^2 = 0.1$.

Figure 8 shows lateral variations behind the projectile in the maxa and minima of the induced potential at $\rho = 0$. The difference in decay length between the two extremes, $\omega_p^2/\omega_0^2 = 10$ and 0.1 follows the difference in the corresponding periods in figure 6, while the variation in decay length from maximum to maximum or from minimum to minimum appears insignificant.

5.3 Charge Dependence

We have also studied the dependence of the induced field on the ion charge $q_1 e$. The potential of the screened projectile charge has been expressed by a rather common expression [21],

$$V(r) = \frac{q_1 e}{r} + \frac{(Z_1 - q_1)e}{r} e^{-r/a}, \tag{14}$$

and for the screening radius a we have adopted the expression [22]

$$a = (1 - q_1/Z_1)\, a_{TF} = (1 - q_1/Z_1)\, 0.8853 a_0/Z_1^{1/3}, \tag{15}$$

a choice that has also been adopted in the PASS code [23].

Screening enters the integrand in eq. (9) as an additional factor

$$f(k, a, \beta) = \frac{k^2a^2 + q_1/Z_1}{k^2a^2 + 1}. \tag{16}$$

The two graphs in the upper row of figure 9 refer to the Fermi gas (left) and an oscillator gas with $\omega_p^2/\omega_0^2 = 10$, i.e., high electron density. As expected, the graphs are very similar, and the magnitude of the induced field decreases with decreasing charge. This implies *weaker* screening of the field in the vicinity of the projectile as the charge decreases, and a strong suppression of the oscillatory potential far behind it.

Similar, slightly reduced features are still found for $\omega_p^2/\omega_0^2 = 1$, whereas the graph referring to low density or $\omega_p^2/\omega_0^2 = 0.1$ shows only a barely visible screening effect of the potential near the projectile, but a surprisingly weak dependence of the far field on the ion charge.

6 Inner and Outer Electron Shells

In order to extract some implications on real systems we need to consider multiple-electron target atoms. We may get a hint from the long-wavelength limit of the dielectric function,

$$\epsilon(\omega) = 1 + \omega_p^2 \sum_j \frac{f_j}{\omega_j^2 - \omega^2 - i\gamma_j\omega}, \qquad \sum_j f_j = 1, \tag{17}$$

which is a straight extension of the Drude-Lorentz function to a multi-electron atom characterized by resonance frequencies ω_j and oscillator strengths f_j. Here ω_p^2 is determined by the *total* electron density of the target material. We may write eq. (17) in an alternative way,

$$\epsilon(\omega) = 1 + \sum_j \frac{\omega_{pj}^2}{\omega_j^2 - \omega^2 - i\gamma_j\omega}, \tag{18}$$

where

$$\omega_{pj}^2 = \omega_p^2 f_j = \frac{4\pi N_j e^2}{m} \tag{19}$$

with

$$N_j = N Z_2 f_j, \tag{20}$$

where N is the number of atoms per volume, Z_2 the number of electrons on a target atom and $N_j = Z_2 f_j$ the number of j-electrons per volume.

With this, the function $1/\epsilon(\omega) - 1$ has the same form as eq. (18), except that the resonance frequencies are shifted. This implies that polarization fields add up linearly within this approximation, albeit modified due to shifted resonance frequencies. For qualitative orientation we may ignore these shifts.

Under the above assumptions, a single electron shell is characterized by a plasma frequency ω_{pj}, eq. (19) and a resonance frequency ω_{0j} which, very roughly, may be approximated by

$$\hbar\omega_{0j} \simeq \frac{{Z_j'}^2 e^2}{2n_j^2 a_0}, \tag{21}$$

where Z'_j is the effective charge determining the motion of a j-electron. With this we find

$$\frac{\omega_{pj}^2}{\omega_{0j}^2} \simeq \frac{12}{D^3} Z_j \left(\frac{n_j}{Z'_j}\right)^4, \tag{22}$$

where $Z_j = Z_2 f_j$ and D is a dimensionless measure of the internuclear distance in the material defined by

$$\frac{4\pi}{3} N (Da_0)^3 = 1, \tag{23}$$

i.e., typically $D = 3 - 4$.

For a given material, with Z_2 and D fixed, the behavior of the ratio $\omega_{pj}^2/\omega_{0j}^2$ is governed by the factor $(n_j/Z'_j)^4$, which increases rapidly from $1/Z_2^4$ for the K shell to some value of the order of ~ 1 in the outermost shell. The factor $12/D^3 \sim 1/3$ in the front is roughly constant for most solid materials, whereas Z_j increases monotonically, except for the outermost shell.

Thus, the present results do not suggest to challenge the assumption underlying more or less implicitly the existing literature, that wake phenomena are associated with weakly-bound target electrons. Therefore a description in terms of only two frequencies appears meaningful to analyse wake phenomena in real solids.

In a free-electron metal, where the ratio ω_p^2/ω_0^2 is normally $\gg 1$, figures 6, 7 and 9 indicate that a description in terms of a Fermi-gas model of the solid, with ω_p determined by the number of conduction electrons, should be adequate. In insulators, an effective resonance frequency ω_0 may be defined if a distinct low-frequency part can be identified in the oscillator-strength spectrum. The pertinent plasma frequency is then given by the number of electrons contained in that part of the spectrum.

7 Implications

As mentioned in the introduction, wake phenomena in the nonrelativistic regime have been discussed primarily in connection with the penetration of molecular and cluster ions. For pertinent reviews we refer to refs. [9] and [24]. Here we focus on the energy loss of molecular ions.

Measurements with H_2^+ and H_3^+ ions indicated enhanced energy losses per atom as compared to the stopping of isolated H ions [25]. Recent measurements [26] indicate that the enhancement is smaller than reported in ref. [25], but the existence of the effect is well established by numerous existing data [24]. There is also common agreement that enhanced stopping is due to enhanced energy transfer to target electrons, while diminished stopping, which has been found for heavier molecular ions [27], has been ascribed to a charge-state effect [28–30].

Estimates of enhanced stopping have commonly been based on the Lindhard formalism [10], with the projectile being represented by the charge distribution of a molecule or cluster either at a fixed orientation or averaged over random orientations [24, 31]. This has given rise to the widely-spread view that it is the wake force that causes enhanced or diminished energy losses. As one of numerous examples we mention a statement in a recent paper [32] that 'The wake forces between fragments ... are the main responsible for the vicinage effects in the energy loss'. On the other hand, in ref. [33] we have shown that relative enhancements in stopping increase monotonically with *decreasing* target density, i.e., the *relative* enhancement is greatest when there is no wake at all. Since it appears difficult to reconcile these two views, we need to go into some detail.

Let us first note that energy loss to target electrons has an interaction range $\simeq v/\omega$, i.e., the adiabatic radius [34], where ω is a representative resonance frequency for the outermost electrons. Therefore, there is general agreement that proximity effects in energy loss are negligible if the internuclear distance exceeds this radius. In the present context we have

$$\omega \simeq \sqrt{\omega_p^2 + \omega_0^2}, \tag{24}$$

where ω_0 is the resonance frequency of the outermost shell of an isolated target atom. If inner shells cannot be neglected, ω is even greater.

The abscissa variables in figures 6 and 7 being $\omega_p x/v$ and $\omega_p \rho/v$, respectively, the pertinent range of interest is given by

$$\left|\frac{\omega_p x}{v}\right| \lesssim \frac{\omega_p}{\omega} < 1 \tag{25}$$

$$\left|\frac{\omega_p \rho}{v}\right| \lesssim \frac{\omega_p}{\omega} < 1. \tag{26}$$

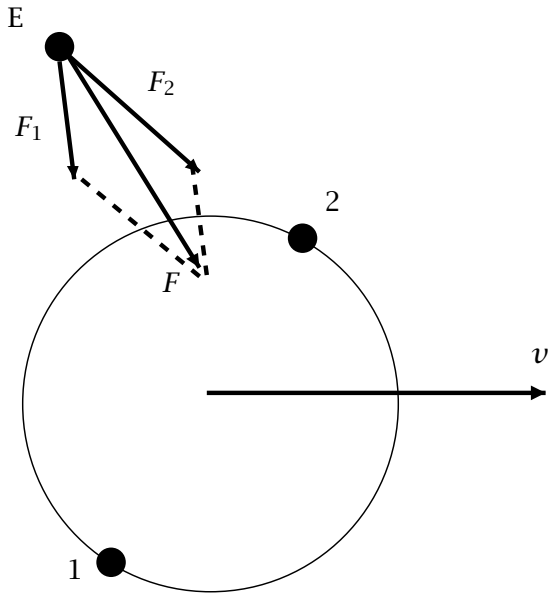

Fig. 11. Domains in molecule penetration. See text

7.1 Analysis via Bohr's Picture

Now consider a molecule of an arbitrary orientation penetrating through some material. Figure 11 shows the action

on a target electron E of a molecule 12 moving with a velocity v. If we neglect induced potentials, the central forces $\boldsymbol{F}_1$ and $\boldsymbol{F}_2$ result in momentum transfers $\boldsymbol{P}_1$ and $\boldsymbol{P}_2$ and, hence, a kinetic-energy transfer $(\boldsymbol{P}_1+\boldsymbol{P}_2)^2/2m$. This quantity exceeds the individual energy transfers $(P_1^2 + P_2^2)/2m$ if $\boldsymbol{P}_1 \cdot \boldsymbol{P}_2 > 0$. This condition is fulfilled for all electrons outside the circle connecting the two nuclei in the figure.

Evidently, the relative contribution to stopping by electrons outside the circle increases as the ratio between the adiabatic radius and the internuclear distance in the molecule increases.

In a dense medium, it is the sum of the two potentials as well as the two induced potentials that act on the target electron. As a first consequence the respective forces $\boldsymbol{F}_1$ and $\boldsymbol{F}_2$ get smaller as the induced potential increases, and so does the relative enhancement in stopping, as was shown in ref. [33]. An exception is found for molecules aligned with the beam direction, where the range of the effective interaction potential gets extended, so that both positive and negative enhancements become possible [24, 31].

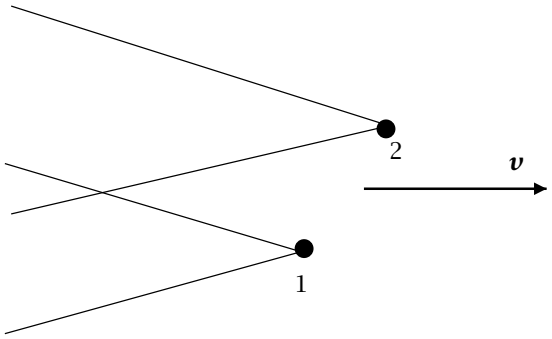

Fig. 12. Both atoms outside each other's Mach-cones. See text

7.2 Analysis via Fermi's View

According to Fermi, the energy loss per pathlength of a point charge is given by the gradient of the induced potential at the position of the particle, multiplied with its charge [1, 4, 10]. In this picture, the force on atom 1 in a dicluster is given by the sum of its induced force, $\boldsymbol{F}_{11}^{\rm ind}$, the force $\boldsymbol{F}_{21}$ from atom 2 in the absence of the medium and the induced force $\boldsymbol{F}_{21}^{\rm ind}$ from atom 2. With this, the force on the molecule is

$$\boldsymbol{F} = \boldsymbol{F}_{11}^{\rm ind} + \boldsymbol{F}_{22}^{\rm ind} + \boldsymbol{F}_{21}^{\rm ind} + \boldsymbol{F}_{12}^{\rm ind}, \qquad (27)$$

since $\boldsymbol{F}_{21} + \boldsymbol{F}_{12} = 0$.

While $\boldsymbol{F}_{11}^{\rm ind}$ and $\boldsymbol{F}_{22}^{\rm ind}$ are directed along the (negative) beam direction, $\boldsymbol{F}_{21}^{\rm ind}$ and $\boldsymbol{F}_{12}^{\rm ind}$ have both lateral and longitudinal components. It is the latter that govern energy loss, while the former contribute to multiple scattering. Thus, a positive enhancement of the stopping force is found for

$$\boldsymbol{F}_{21,x}^{\rm ind} + \boldsymbol{F}_{12,x}^{\rm ind} < 0, \qquad (28)$$

where x denotes the beam direction.

Equation (28) is certainly fulfilled for a dicluster oriented perpendicular to the beam, as is evident e.g. from figure 1. It is also fulfilled in a configuration sketched in figure 12. It is well known, although not very clear from our 3D graphs, that the oscillatory part of the induced potential is confined by a Mach-type cone. Outside this cone the induced potential is attractive. Figure 13 shows a contour plot of the induced potential plotted in figure 1, upper graph.

Clearly, enhanced stopping is determined by the wake field in this picture, but so is basic atomic stopping. Or conversely: If there is no wake, not only is there no enhanced stopping: There is no stopping at all.

Now, consider an electron gas (free or bound) at a certain density. If that density decreases, the induced field gets smaller. This affects both $\boldsymbol{F}_{11}$ and $\boldsymbol{F}_{21}$ and the corresponding forces acting on atom 2. However, $\boldsymbol{F}_{21}$ decreases more slowly, since the screening radius v/ω' gets larger. Hence the proximity effect increases with decreasing electron density, in agreement with ref. [33].

7.3 Microscopic and macroscopic quantities

Evidently, the proximity effect is related to the induced field. Does this imply that it is caused by the wake field?

Consider a dilute gas, where [20]

$$\frac{1}{\epsilon} - 1 \simeq -4\pi\chi, \qquad (29)$$

where χ, the susceptibility is related to the atomic polarizability γ as $\chi = N\gamma$.

Now, within the range of validity of eq. (29), the ratio F_{21}/F_{11} and, therefore, the stopping ratio R – i.e., the ratio between the stopping force on the cluster and the sum of the stopping forces on the constituents – becomes independent of the density N. *Thus, for a dilute gas the stopping ratio is a microscopic parameter independent of the density of the medium.* In contrast, the wake field is a macroscopic quantity which vanishes in the limit of $N = 0$.

We conclude that the frequently-expressed view that the proximity effect in energy loss should be *caused* by the polarization wake is not tenable. The wake potential *influences* the proximity effect, but that effect is greatest for binary collisions in vacuum where there is no wake at all.

Interestingly, the claim of the wake being the cause of the proximity effect has not been made in the pioneering papers [25, 31], nor did we find it in a major review [12]. However, we did find an early explicit statement in ref. [35], which seems to have triggered numerous subsequent ones, including the one quoted above from ref. [32].

This work has been supported by the Danish Natural Science Research Council (FNU).

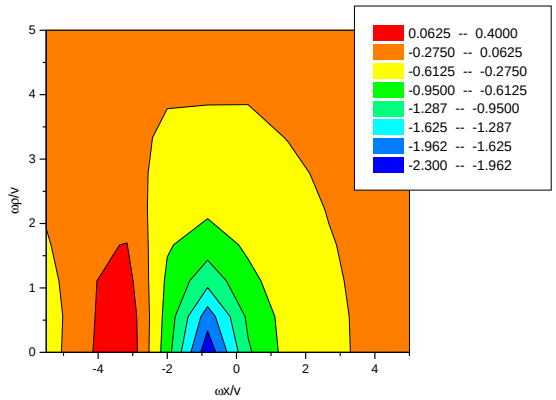

Fig. 13. Contour plot of figure 1, top graph.

References

1. E. Fermi, Phys. Rev. 57 (1940) 485.
2. N. Bohr, Mat. Fys. Medd. Dan. Vid. Selsk. 18 no. 8 (1948) 1.
3. H. A. Kramers, Physica 13 (1947) 401.
4. A. Bohr, Mat. Fys. Medd. Dan. Vid. Selsk. 24 no. 19 (1948) 1.
5. J. Neufeld and R. H. Ritchie, Phys. Rev. 98 (1955) 1632.
6. V. N. Neelavathi, R. H. Ritchie and W. Brandt, Phys. Rev. Lett. 33 (1974) 302.
7. W. Brandt and R. H. Ritchie, Nucl. Instrum. Methods 132 (1976) 43 .
8. Z. Vager and D. S. Gemmell, Phys. Rev. Lett. 37 (1976) 1352.
9. D. S. Gemmell, Nucl. Instrum. Methods 194 (1982) 255.
10. J. Lindhard, Mat. Fys. Medd. Dan. Vid. Selsk. 28 no. 8 (1954) 1.
11. P. M. Echenique, R. H. Ritchie and W. Brandt, Phys. Rev. B 20 (1979) 2567.
12. P. M. Echenique, F. Flores and R. H. Ritchie, Sol. State Phys. 43 (1990) 229.
13. I. Abril, R. Garcia-Molina, C. Denton, F. J. Pérez-Péres and N. R. Arista, Phys. Rev. A 58 (1998) 357 .
14. V. H. Ponce, F. J. Fuhr, J. D. Valdés and F. J. G. de Abajo, Nucl. Instrum. Methods B 146 (1998) 11.
15. I. Campillo and J. M. Pitarke, Nucl. Instrum. Methods B 164 (2000) 161.
16. H. Esbensen and P. Sigmund, Ann. Physics N.Y. 201 (1990) 152.
17. A. Belkacem and P. Sigmund, Nucl. Instrum. Methods B 48 (1990) 29.
18. P. Sigmund and U. Haagerup, Phys. Rev. A 34 (1986) 892.
19. M. Abramowitz and I. A. Stegun, *Handbook of mathematical functions* (Dover, New York, 1964).
20. J. D. Jackson, *Classical electrodynamics* (John Wiley & Sons, New York, 1975).
21. W. Brandt and M. Kitagawa, Phys. Rev. B 25 (1982) 5631.
22. P. Sigmund, Phys. Rev. A 56 (1997) 3781.
23. P. Sigmund and A. Schinner, Nucl. Instrum. Methods B 195 (2002) 64.
24. N. R. Arista, Nucl. Instrum. Methods B 164-165 (2000) 108.
25. W. Brandt, A. Ratkowski and R. H. Ritchie, Phys. Rev. Lett. 33 (1974) 1325.
26. S. M. Shubeita, P. L. Grande, J. F. Dias, R. Garcia-Molina, C. D. Denton and I. Abril, Phys. Rev. B 83 (2011) 245423.
27. M. F. Steuer, D. S. Gemmell, E. P. Kanter, E. A. Johnson and B. J. Zabransky, Nucl. Instrum. Methods 194 (1982) 277.
28. J. Jensen and P. Sigmund, Phys. Rev. A 61 (2000) 032903.
29. Z. L. Miskovic, W. K. Liu, F. O. Goodman and Y. N. Wang, Phys. Rev. A 64 (2001) 064901.
30. S. Heredia-Avalos, R. Garcia-Molina and N. R. Arista, Europhys. Lett. 54 (2001) 729.
31. N. R. Arista, Phys. Rev. B 18 (1978) 1.
32. S. M. Shubeita, R. C. Fadanelli, J. F. Dias, P. L. Grande, C. D. Denton, I. Abril, R. Garcia-Molina and N. R. Arista, Phys. Rev. B 80 (2009) 205316.
33. P. Sigmund and A. Schinner, Europ. Phys. J. D 61 (2011) 39.
34. N. Bohr, Philos. Mag. 25 (1913) 10.
35. J. C. Eckardt, G. Lantschner, N. R. Arista and R. A. Baragiola, J. Phys. C 11 (1978) L851.

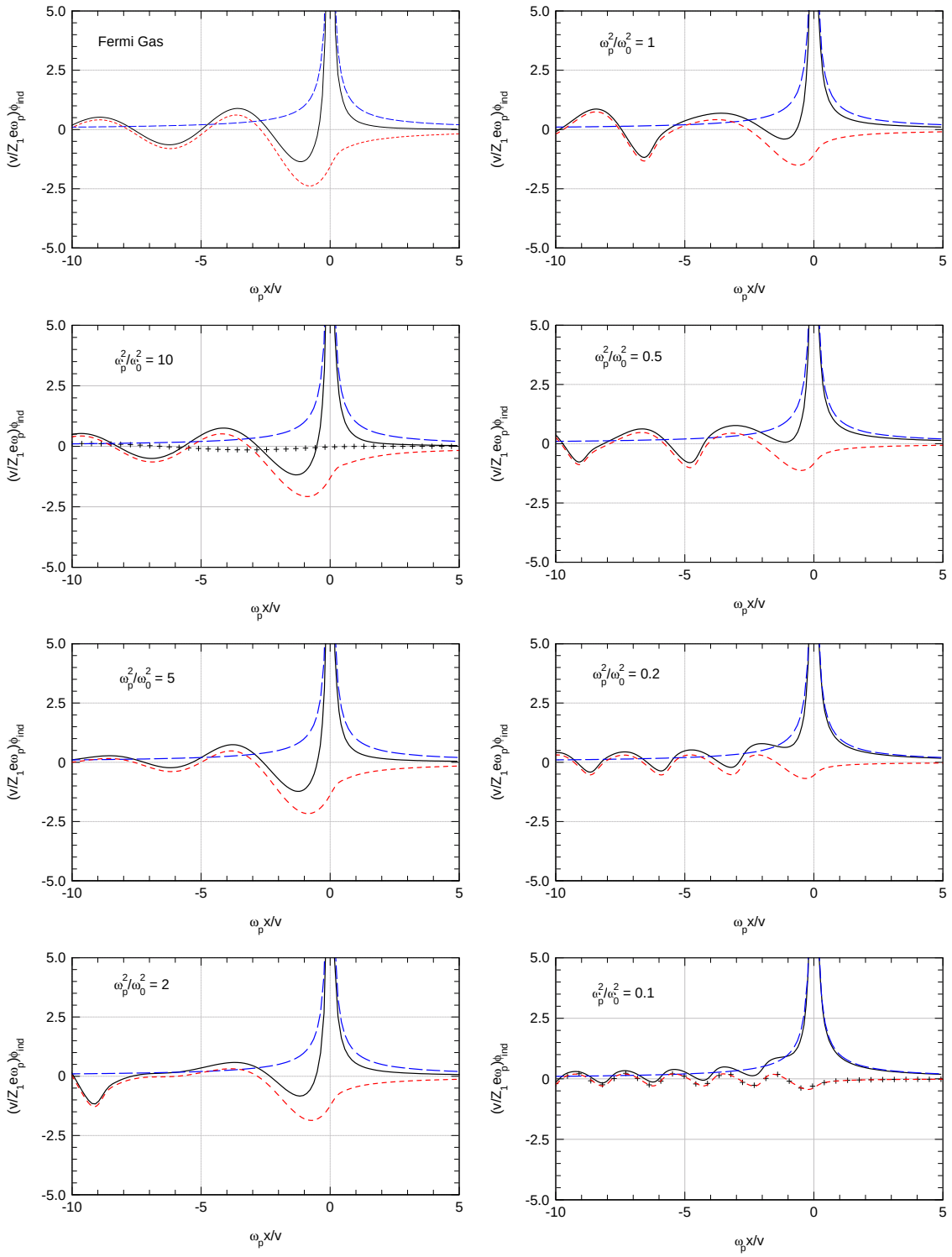

Fig. 6. Induced potential (red dotted lines), Coulomb potential (blue dashed lines) and total potential (solid black lines) at $\rho = 0$ for $B = 2mv^2/\hbar\omega_p = 10$. Crosses denote the induced potential approximated by the first term ($j = 1$) in eq. (9). Results for the Fermi gas at $r_s = 2$ (top left) and for an ensemble of oscillators for $\omega_p^2/\omega_0^2 = 10$ to 0.1.

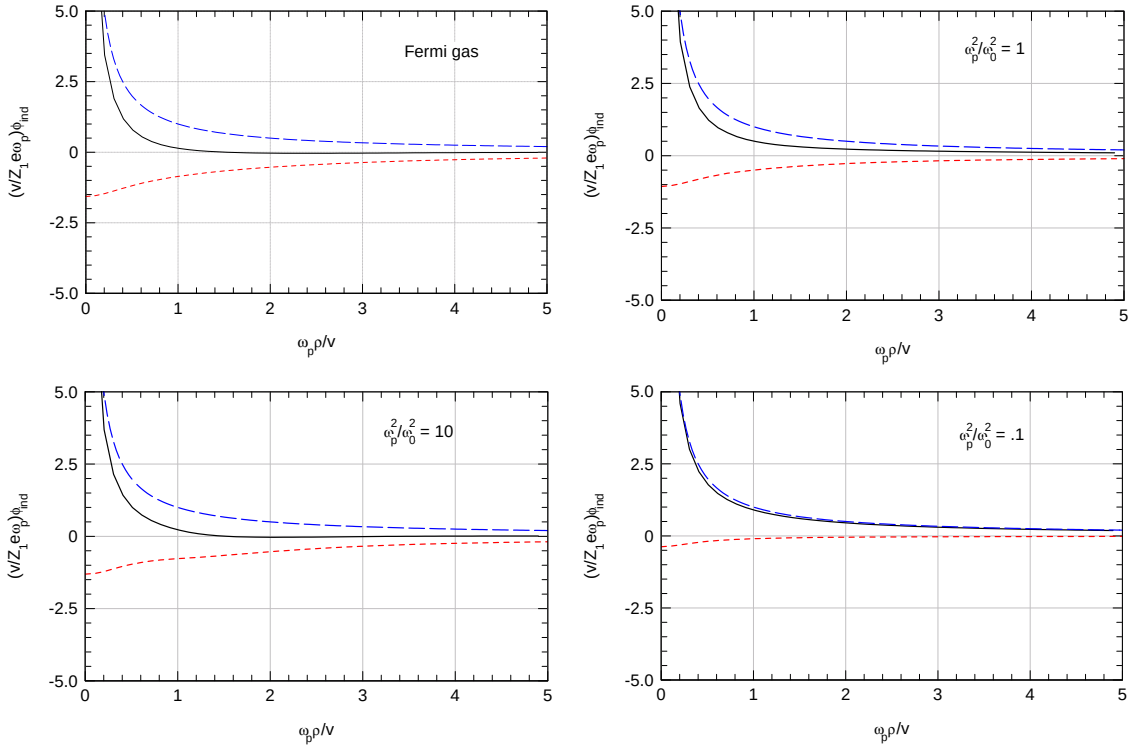

Fig. 7. Same as figure 6 for $x = 0$ and variable ρ.

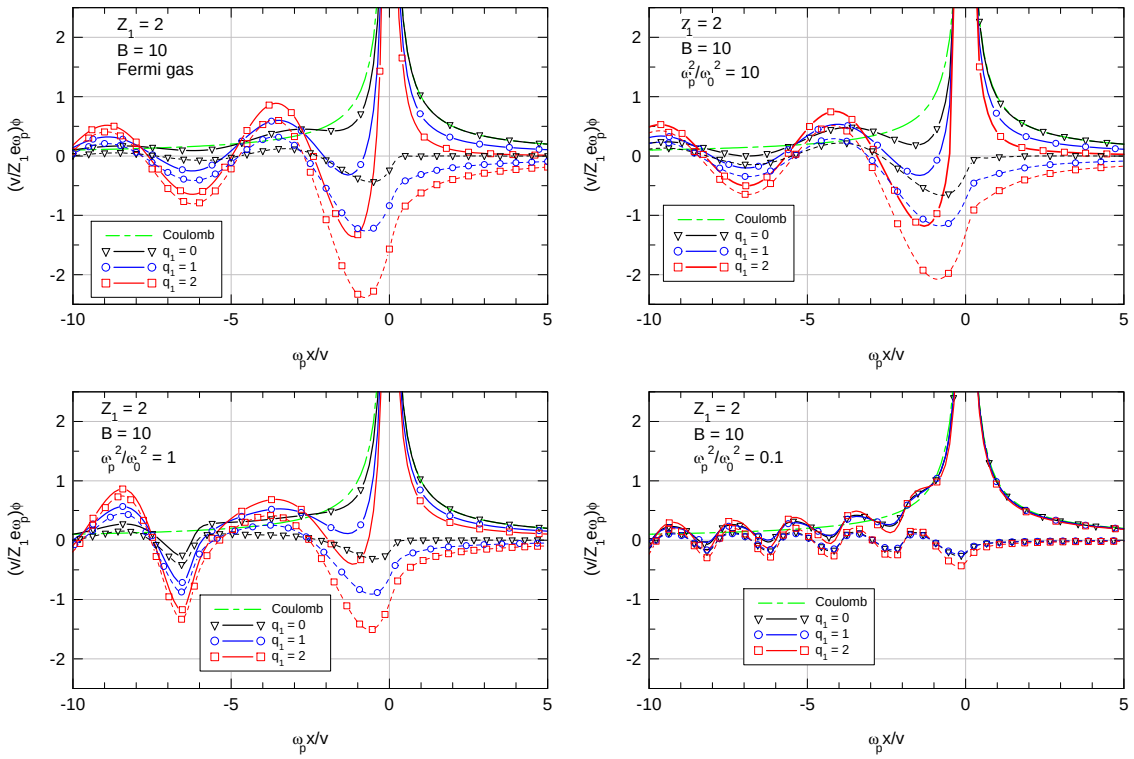

Fig. 9. Charge-state dependence: Dashed lines: induced potential. Solid lines: Total potential; Dot-dashed line: Bare Coulomb potential. Fermi gas (top left) and oscillator model; $B = 2mv^2/\hbar\omega_p = 10$; $Z_1 = 2; \hbar\omega_0 = 13.6$ eV. $\omega_p^2/\omega_0^2 = 10$, 1 and 0.1.

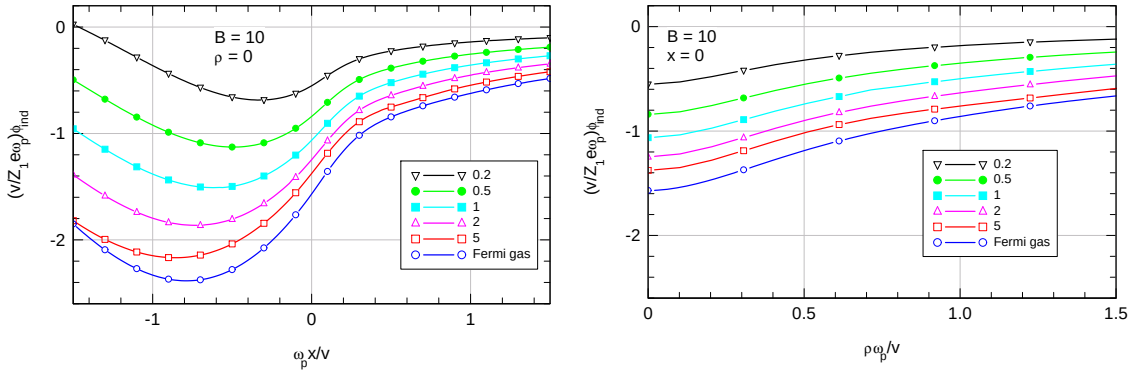

Fig. 10. Induced potentials from figure 6 (top) and figure 7 (bottom) in the near-field regime.